

Three-dimensional seismic structure and moment tensors of non-double-couple earthquakes at the Hengill–Grensdalur volcanic complex, Iceland

A. D. Miller,¹ B. R. Julian² and G. R. Foulger¹

¹Department of Geological Sciences, Science Laboratories, South Road, Durham, DH1 3LE, UK

²US Geological Survey, 345, Middlefield Road, MS 977, Menlo Park, CA 94025, USA

Accepted 1997 November 4. Received 1997 November 3; in original form 1997 May 9

SUMMARY

The volcanic and geothermal areas of Iceland are rich sources of non-double-couple (non-DC) earthquakes. A state-of-the-art digital seismometer network deployed at the Hengill–Grensdalur volcanic complex in 1991 recorded 4000 small earthquakes. We used the best recorded of these to determine 3-D V_p and V_p/V_s structure tomographically and accurate earthquake moment tensors. The V_p field is dominated by high seismic wave speed bodies interpreted as solidified intrusions. A widespread negative (–4 per cent) V_p/V_s anomaly in the upper 4 km correlates with the geothermal field, but is too strong to be caused solely by the effect of temperature upon liquid water or the presence of vapour, and requires in addition mineralogical or lithological differences between the geothermal reservoir and its surroundings. These may be caused by geothermal alteration. Well-constrained moment tensors were obtained for 70 of the best-recorded events by applying linear programming methods to P - and S -wave polarities and amplitude ratios. About 25 per cent of the mechanisms are, within observational error, consistent with DC mechanisms consistent with shear faulting. The other 75 per cent have significantly non-DC mechanisms. Many have substantial explosive components, one has a substantial implosive component, and the deviatoric component of many is strongly non-DC. Many of the non-DC mechanisms are consistent, within observational error, with simultaneous tensile and shear faulting. However, the mechanisms occupy a continuum in source-type parameter space and probably at least one additional source process is occurring. This may be fluid flow into newly formed cracks, causing partial compensation of the volumetric component. Studying non-shear earthquakes such as these has great potential for improving our understanding of geothermal processes and earthquake source processes in general.

Key words: earthquakes, geothermal processes, Hengill–Grensdalur volcanic complex, Iceland, moment tensors, seismic structure.

1 INTRODUCTION

The Hengill–Grensdalur volcanic complex lies at a ridge–ridge–transform triple junction on the plate boundary in SW Iceland (Fig. 1). The structure and evolution of the area is described by various authors (e.g. Foulger 1988a; Foulger & Toomey 1989; Saemundsson 1995a). The currently active spreading plate boundary is represented by the Hengill volcanic system, a NNE-striking swarm of normal faults and fissures containing the Hengill central volcano (Fig. 2). The area is complicated as a consequence of a recent (~ 0.5 Ma) westerly ridge jump of about 5 km. The earlier locus of spreading now forms the extinct Grensdalur volcanic system, which lies about

8 km ESE of the Hengill system (Fig. 2). A third system, the Hrómundartindur system, lies between the Hengill and Grensdalur systems. This system formed simultaneously with the Hengill system, but remained subsidiary and is now inactive.

This triplet of volcanic systems is encompassed by a high-temperature geothermal area that covers an area of 70 km² (Saemundsson 1995b). The natural heat loss is about 350 MW and commercial exploitation is underway at Nesjavellir, NNE of the Hengill volcano. Over 20 wells up to 2.5 km deep have been drilled for steam and hot water for electricity generation and space heating in Reykjavik.

Cooling, mostly due to natural heat loss, and consequential thermal contraction and cracking in the heat source, are

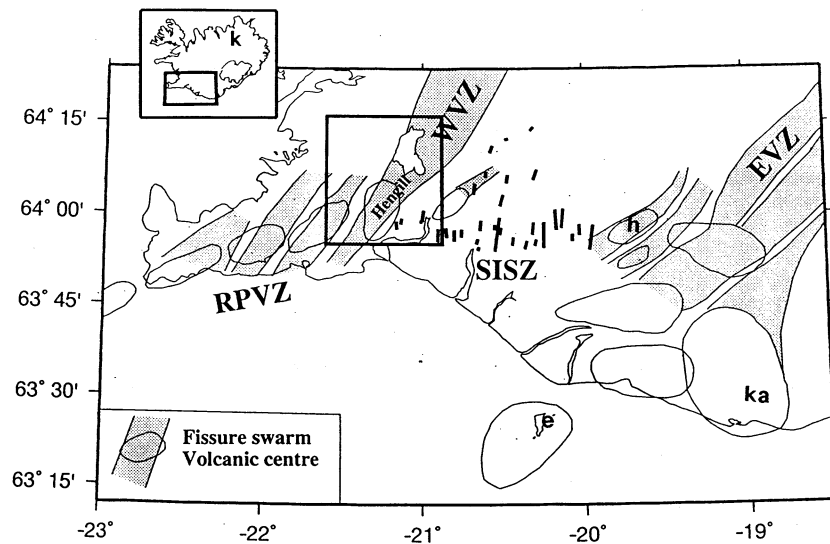


Figure 1. Location of the Hengill–Grensdalur volcanic complex in SW Iceland. The area is a triple junction formed by the South Iceland Seismic Zone (SISZ), the Western Volcanic Zone (WVZ) and the Reykjanes Peninsula Volcanic Zones (RPVZ). EVZ: Eastern Volcanic Zone; k: Krafla; h: Hekla; ka: Katla; e: Eldfell; short black lines: right-lateral strike-slip faults of the SISZ. Box: area shown in Fig. 2.

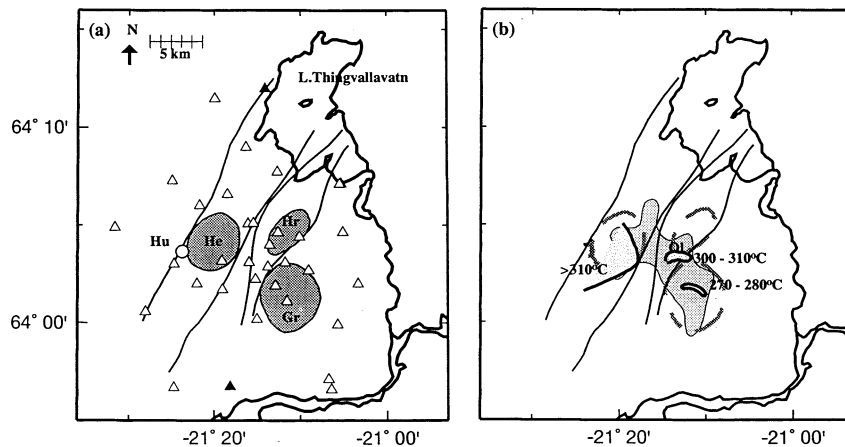


Figure 2. Maps of the Hengill–Grensdalur area. (a) Grey shading: the Hengill (He), Hrómundartindur (Hr) and Grensdalur (Gr) volcanic centres; thin lines: outlines of the Hengill and Hrómundartindur fissure swarms; Hu: the Húsmúli basalt shield; open triangles: temporary stations deployed in 1991; filled triangles: stations of the permanent South Iceland Lowland seismic network. (b) Grey shading: the geothermal area. Also indicated are areas where reservoir temperature highs have been determined using fumarole geochemistry (Torfason *et al.* 1983).

thought to be responsible for the continuous small-magnitude earthquake activity in the area. This mode of earthquake induction was suggested following the observation that many of the earthquakes have severely non-double-couple (non-DC) focal mechanisms with large explosive components (Foulger & Long 1984; Foulger 1988b). The source process was hypothesized to be partially compensated tensile cracking.

The abundant local earthquake activity was used to study subsurface structure using local earthquake tomography (LET). P -wave arrival times were measured from earthquakes recorded on a temporary network of vertical-component, analogue instruments deployed in 1981 (Toomey & Foulger 1989; Foulger & Toomey 1989). The V_p structure found correlates with surface geology. Most prominent are high-wave-speed bodies associated with the inactive Grensdalur and Hrómundartindur volcanic centres. These were interpreted as hot but solidified intrusions that fuel the geothermal area above. The currently active Hengill volcanic system is devoid

of such bodies, but a small, low-wave-speed body was found beneath the NE flank of the volcano and was tentatively interpreted as a magma body.

The earthquake radiation patterns were well constrained, and contributed greatly to the recognition that not all earthquakes have DC mechanisms. Detailed understanding of the source physics was impossible, however, partly because only analogue, vertical-component seismograms were available and thus only suites of candidate moment tensors based on P -wave polarities could be determined. For this reason, we revisited the area in 1991 and deployed a state-of-the-art network and obtained three-component digital recordings of several thousand earthquakes.

We used the new data set to conduct V_p and V_p/V_s LET and to determine earthquake moment tensors by applying linear programming methods to P - and S -wave polarities and amplitude ratios. The V_p model largely confirms the results of the earlier tomographic study. The V_p/V_s model

shows variations that correlate with the geothermal resources, suggesting that V_p/V_s LET is potentially useful for geothermal exploration. In the moment tensor analysis, we corrected for 3-D heterogeneity by tracing rays through the tomographic model to observations onto the focal sphere. The moment tensors obtained cannot be explained solely by the earlier model of compensated tensile faulting. Many events are consistent with combined shear and tensile faulting, but others require some additional process, which could be fluid flow causing volumetric compensation. Short summaries of some of the main results have been presented by Foulger *et al.* (1995) and Julian, Miller & Foulger (1997). This paper presents the detailed 3-D structures derived from the tomographic inversion, a quantitative interpretation of the V_p/V_s anomaly, and moment tensors for 70 of the best-recorded earthquakes.

2 THE FIELD SURVEY

The network deployed in the Hengill–Grensdalur area in 1991 comprised 30 seismic stations and was operated for two months (Fig. 2). The seismometers used were Mark Products model L22D, three-component instruments with natural frequencies of 2 Hz, plastered onto bedrock in the bottoms of shallow pits. REFTEK model 72A data loggers digitized the seismic signals at 100 sps per component and, because of the prohibitive cost of digital radio transmitters, data were recorded at each station on field disks. Power was provided by lead–acid batteries. Two triggering digital stations of the permanent Icelandic network provided supplementary data. All the station locations were determined using differential GPS to an accuracy of about 1 m.

The most carefully tuned event-detection algorithms miss at least 20 per cent of interesting events when detection is conducted independently at individual stations (J. Evans, personal communication, 1991). In the case of temporary networks, a lack of prior knowledge of noise and signal conditions may increase this data-loss rate to 50 per cent. Therefore, we recorded continuously, and as a result about 50 Mbytes of data per day were collected at each station. The majority of the field disks available to us in 1991 had capacities of 170 Mbyte, and the rest had capacities of 660 Mbyte. Most of the stations thus had to be serviced every three days.

Prior to network deployment, we traced rays through the V_p structure obtained from the earlier tomographic study (Toomey & Foulger 1989) and used the results to select station sites that provided uniform coverage of the focal sphere for earthquakes in the central, most active, part of the area (Foulger 1988a) (Fig. 3). This strategy yielded optimal data for moment tensor determination but, because the terrain of the area is very rugged, many stations were consequently sited in areas of difficult access and had to be serviced by foot. This, coupled with our continuous-recording policy resulted in an extremely arduous field survey in which we walked 1700 km, many of them carrying 25 kg batteries in addition to disks and spares.

We detonated a 10 kg explosion at a depth of 10 m in a lake in the centre of the network to verify the polarity of the seismometers. This explosion was recorded with large-amplitude motions at all stations of our network. Despite the fact that all the instruments and recorders were of the same manufacture, and we had the usual firm assurances that they all had the same response, 25 per cent of the stations recorded downward first motions and 75 per cent recorded upward

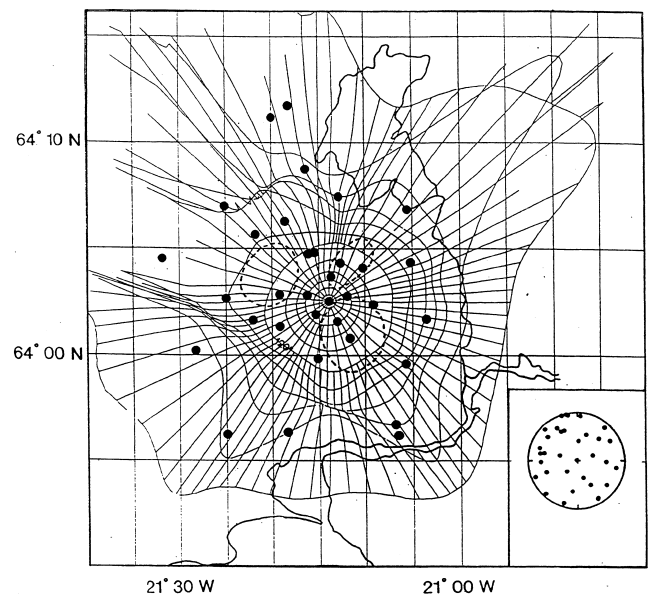


Figure 3. Map view of rays traced through the 3-D wave-speed model derived from the 1981 data for an event at 4 km depth beneath the centre of the network. Azimuth and take-off angles (toa) are spaced at 5° intervals for $90^\circ < \text{toa} < 120^\circ$, and at 10° intervals for $120^\circ < \text{toa} < 180^\circ$. Dots: stations deployed in 1991; dashed lines: volcanic centres. Upper-hemisphere, equal-area focal sphere plot of stations is shown at lower right.

motions. (Upward motion is expected at all stations for an explosion.) Failure to detect the reversed polarities of some of our stations would have rendered our data set useless for the primary purpose for which it was intended. This experience thus represents a cautionary tale worthy of record.

The network recorded about 4000 earthquakes, embedded in a continuous data stream with a total volume of ~ 100 Gbytes. In order to facilitate extraction of the events of interest, an event-triggered data stream had also been recorded, and a combined list of trigger times at all the stations was used to identify events. The largest earthquake recorded had a moment of $\sim 2.5 \times 10^3$ Nm ($M \sim 2.7$) and was located south of the Grensdalur volcano.

3 TOMOGRAPHIC INVERSION

3.1 Methodology

Foulger *et al.* (1995) give a brief overview of the procedure and main results of the tomographic inversion. The theory and method are described in detail by a number of authors, e.g. Thurber (1983) and Eberhart-Phillips (1993). The structure is parametrized by the values of V_p and V_p/V_s at the nodes of a 3-D grid, and the observed P - and S -wave arrival times are inverted by an iterative linearized least-squares method to determine simultaneously the hypocentral coordinates and the values of V_p and V_p/V_s at the grid nodes. Trilinear interpolation is used for V_p and V_p/V_s values between the grid nodes.

We measured P - and S -phase arrival times for 228 of the best-recorded earthquakes to accuracies estimated at 0.01 and 0.02 s. Events were selected on the basis of number of arrivals, location, and spatial distribution of the whole set of events. There are an average of 37 arrival times per event, totalling

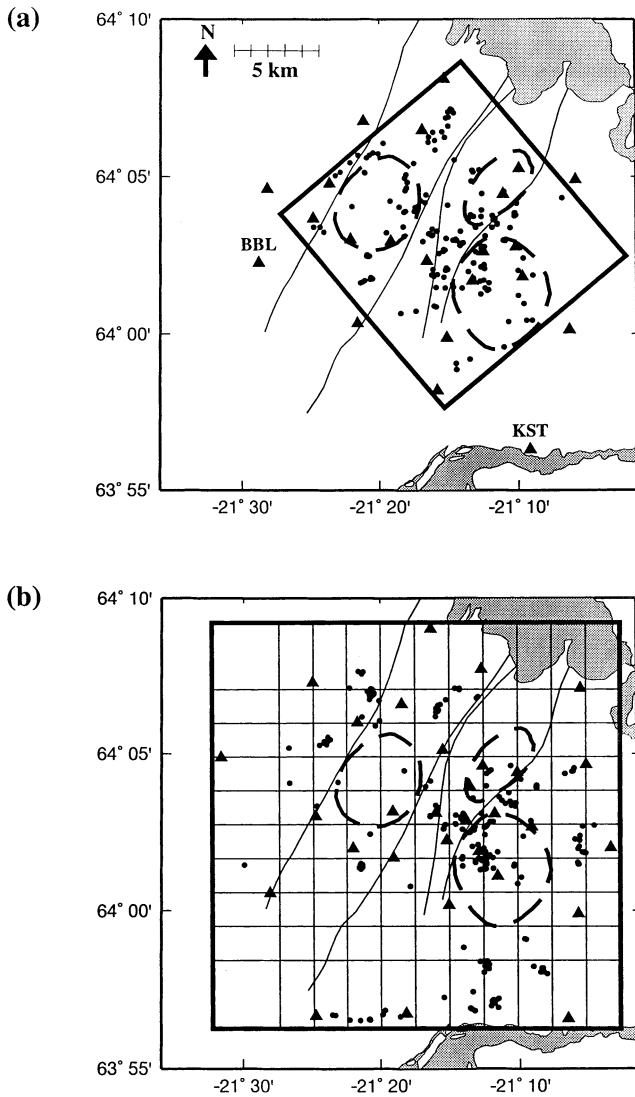


Figure 4. Areas of the low LET studies in the Hengill–Grensdalur area. (a) Area modelled by Toomey & Foulger (1989) using data collected in 1981. (b) Area modelled in this study using data from 1981 and 1991. Triangles: seismic stations; dots: earthquakes used; boxes: outlines of the modelled areas. Nodes are located at the gridline intersections.

4748 P - and 3678 S -arrival times. The 1981 data were added, providing a further 158 earthquakes, 2394 P times and 20 stations (Fig. 4a). The combined data set thus contains 7253 P times, 3678 S times and 55 stations. The 1981 data were given half weight, since they are less accurate and have picking errors of about 0.03 s.

The tomographic inversion started with a 1-D V_P model obtained by inverting the data using the program VELEST (Kissling *et al.* 1994) (Table 1) and an initial V_P/V_S ratio of 1.77, obtained using Wadati diagrams. The grid is $24 \times 24 \times 6$ km in size (Fig. 4b), with nodes spaced at 2 and 4 km in the horizontal and 1 km in the vertical. A single-step inversion yielded the best result. ‘Graded’ strategies, in which a series of inversions are performed using progressively finer grids, adjusting the damping values at each stage, were found to yield extreme lateral wave-speed gradients in the shallowest layers. This behaviour seems to be characteristic of this

Table 1. The best 1-D crustal model for the Hengill–Grensdalur area. Linear wave-speed gradients are assumed within layers.

Depth bsl to top of layer (km)	P -wave speed (km s^{-1})
0.0	2.10
1.0	3.17
2.0	4.35
3.0	5.36
4.0	5.92
5.0	6.22
6.0	6.44
7.0	6.50

particular data set. Other data sets are reported to give better results with graded inversions (e.g. Julian *et al.* 1996). The damping values used were $5 \text{ s}^2 \text{ km}^{-1}$ for V_P and 2 s for V_P/V_S .

The final RMS P and S - P time residuals are 0.023 and 0.037 s, which are close to the expected noise level of the arrival-time measurements. The variance reduction from the 1-D starting model is 53 per cent. The quality of the results was assessed using the spread function (Foulger *et al.* 1995), which measures the degree of local averaging in the computed model. The effect of anisotropy was studied because the traveltimes residuals show a clear azimuthal variation. An empirical approach was taken, where anisotropy was roughly estimated from the residuals and then subtracted from the data. Inversion was performed using these data and the final model obtained was so similar to those using uncorrected data that the conclusions drawn did not alter. The final results using the data uncorrected for anisotropy are shown in Figs 5–8.

3.2 3-D variations in V_P

Several inversions were performed to explore parameter space and the results were found to be largely insensitive to starting model, data set, grid configuration and inversion details (Foulger *et al.* 1995; Miller 1996). This indicates that the structures resolved are strongly supported by the data. The most important structures imaged in the V_P field are laterally extensive high- V_P bodies, with anomalies of $>0.3 \text{ km s}^{-1}$ (up to +12 per cent) from the starting model (Figs 5, 7 and 8). All of these are beneath major extinct volcanic features. A body $\sim 40 \text{ km}^3$ in volume with $\Delta V_P \geq \sim 0.4 \text{ km s}^{-1}$ underlies the Grensdalur volcano in the depth range 1–5 km. A similar body with a volume of $\sim 20 \text{ km}^3$, but limited to the depth range 2–5 km, underlies the most powerful geothermal features in the Hrómundartindur system (Fig. 2b), the Ölkelduhals hot springs. Húsmúli, a prominent basalt shield on the SW flank of the Hengill volcano (Fig. 2), is underlain by a high- V_P body that extends from the surface to at least 4 km depth. Similar results were obtained in inversions using either the 1991 or the 1981 data alone, thus the 1991 and 1981 data are concordant. Wave speeds were depressed by up to 10 per cent in places, but no extensive, coherent, low- V_P bodies were detected using either the combined data set or the 1991 data alone.

3.3 3-D variations in V_P/V_S

The wave-speed ratio V_P/V_S varies by up to ± 4 per cent throughout the area, and the main anomaly is a NW–SE zone

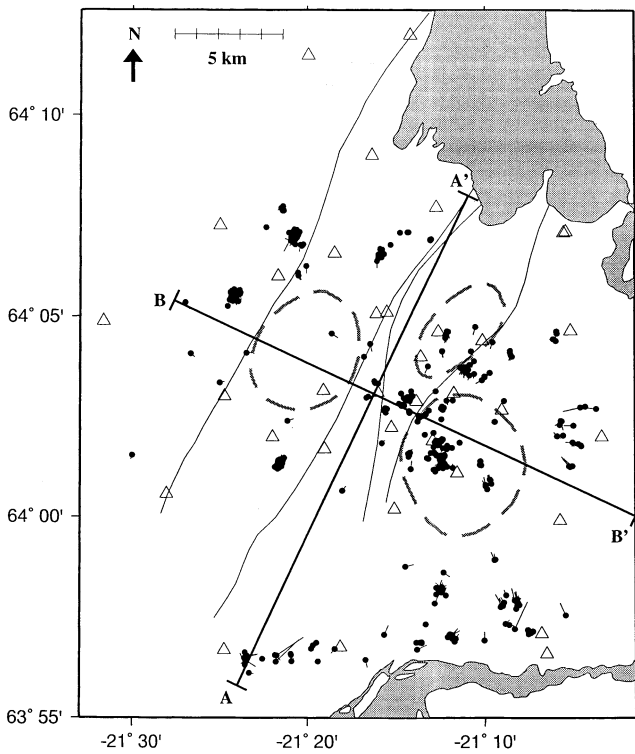


Figure 9. Map of 448 earthquake epicentres (filled circles) determined using the 3-D models. Lines: changes from locations computed from the 1-D model. A-A' and B-B': lines of depth sections shown in Fig. 10. Open triangles: seismometers.

of low V_p/V_s that correlates with the surface geothermal area (Fig. 5). The >2 per cent anomaly persists from near the surface down to ~ 4 km depth (Figs 6, 7 and 8) and is dominated by two vertically extensive zones. One crops out at

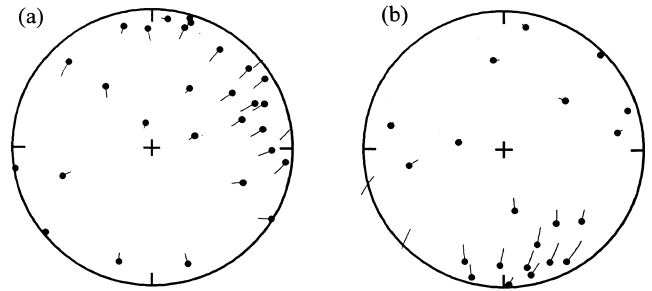


Figure 11. Changes in station positions on the focal sphere computed using 1-D (symbol tail) and 3-D (symbol head) wave-speed models for two events. For event (b) two rays depart downwards for the 1-D model, and are plotted at their antipodal points.

the N and NE boundary of Hengill, just south of the Nesjavellir geothermal wellfield, and in cross-section (Fig. 8) dips towards the SE, that is away from the wellfield and towards the centre of the natural geothermal area. A similar zone crops out in the Grensdalur volcano and dips to the NW so that its deeper levels lie beneath the Ölkelduhals hot springs. Only the deeper parts of the low- V_p/V_s bodies correlate with high- V_p volumes, and whereas the deepest parts of the high- V_p bodies are seismogenic, the low- V_p/V_s bodies are almost entirely aseismic.

3.4 Discussion

Relocating the earthquakes using the 3-D model and the bending method of ray tracing (Julian & Gubbins 1977) resulted in corrections to their locations of up to 1.5 km horizontally and 2.6 km vertically (Figs 9 and 10). The positions of the observations on the focal spheres moved by up to 27° , with a mean of 6° (Fig. 11).

The high- V_p bodies are probably dense, solidified gabbroic intrusions that fed the eruptive sites above when they were

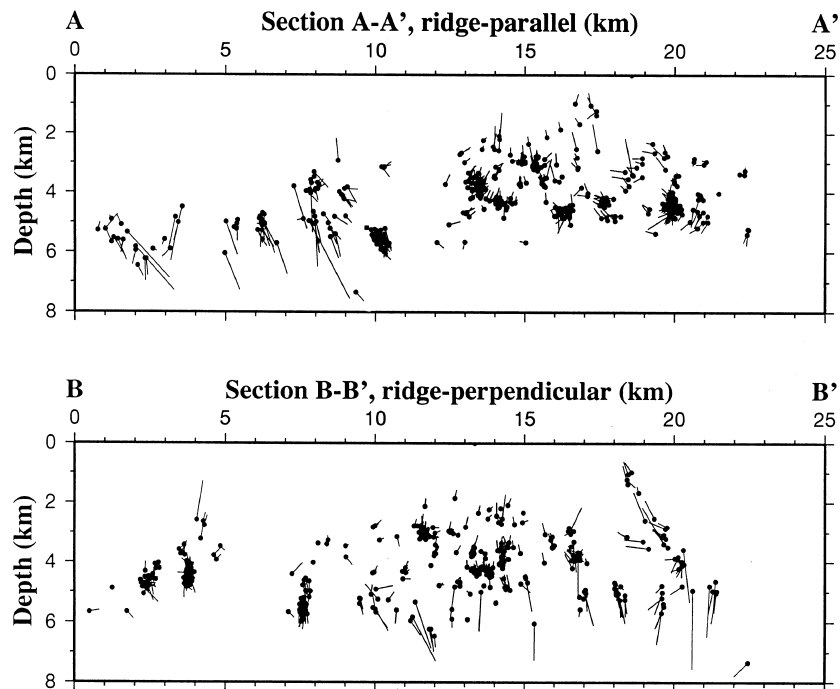


Figure 10. Depth sections, showing hypocentres (filled circles) of earthquakes and changes as in Fig. 9. Lines of section are shown in Fig. 9.

partially molten (Toomey & Foulger 1989). The Grensdalur and Hrómundartindur bodies are seismogenic and thus still hot and cooling (Foulger 1988b). The Húsmúli body is aseismic and thus probably cold. The Húsmúli basalt shield formed at *ca.* 0.1 Ma (Torfason *et al.* 1983), a time consistent with the conclusion that it now contains no geothermal potential.

A small ($\sim 3 \text{ km}^3$) body of low- V_p material beneath the NE part of Hengill was imaged by Toomey & Foulger (1989) using the 1981 data and interpreted as a volume of partial melt. The superior 1991 experiment fails, however, to confirm this. This body was at the limit of resolution of the 1981 data and was probably an artefact of the inversion procedure, which used a very low damping value ($2 \text{ s}^2 \text{ km}^{-1}$) and did not use 'pseudo-bending' ray tracing (Thurber 1993). The currently active Hengill volcanic system appears to be devoid of major V_p anomalies of either sign, indicating that the upper 5 km of this part of the spreading plate boundary is devoid of major intrusions or bodies of partial melt.

A negative V_p/V_s anomaly is typical of many geothermal areas, including Yellowstone (Chatterjee, Pitt & Iyer 1985) and The Geysers, California (O'Connell 1986; Julian *et al.* 1996). They are thought to be caused by changes in the compressibility of the fluid filling rock pores, caused, for example, by variations in temperature or the presence of vapour. Such variations in pore-fluid compressibility strongly affect V_p but not V_s .

To interpret the anomaly quantitatively, we use an empirical relation of the effect of pore-fluid compressibility upon V_p and V_s in saturated rocks (Krief *et al.* 1990; G. Mavko, personal communication, 1997) (Fig. 12). For porosity $\phi = 0$, V_p and V_s have the values of the minerals composing the rock matrix ('Tholeiitic basalt' in Fig. 12). As ϕ increases from 0, V_p^2 and V_s^2 are found to vary nearly along a straight line, towards a point where the effective rigidity modulus μ vanishes (so $V_s = 0$) and the effective bulk modulus K is given by

$$\frac{1}{K} = \frac{\phi_c}{K_f} + \frac{1-\phi_c}{K_0}, \quad (1)$$

where K_0 and K_f are the bulk moduli of the minerals and the fluid respectively, and ϕ_c is a parameter characteristic of the rock. Eq. (1) gives the Reuss average of the bulk moduli of the minerals and the fluid for porosity ϕ_c . Along with the condition $\mu = 0$, it states that the rock behaves as a cohesionless suspension of mineral particles when the porosity reaches ϕ_c .

Application of this empirical theory shows that the V_p/V_s anomaly in the Hengill–Grensdalur area cannot result solely from variations in the compressibility of the pure fluid. Fig. 12 shows lines computed for basalt of tholeiitic composition with liquid-water pore fluid at different temperatures (300°C , near the boiling point, and 200°C) and with water-vapour pore fluid, all at a pressure of 12.5 MPa (125 bars), corresponding to hydrostatic pressure at about 1.3 km depth. An infinitely compressible pore fluid (vacuum) would correspond to a line visually indistinguishable from the vapour line on Fig. 12.

All these lines pass close to the elastic-wave speeds observed outside (point A) and inside (point B) the V_p/V_s anomaly, and slight changes in the assumed mineral moduli could cause any of the lines to pass through either of the points that represent the observations. No such changes, however, can make the separation between the lines as large as the vertical separation of the two points. Certainly, temperature is high and pore fluid is relatively compressible beneath the geothermal area, and this compressibility must cause a V_p/V_s anomaly. The total

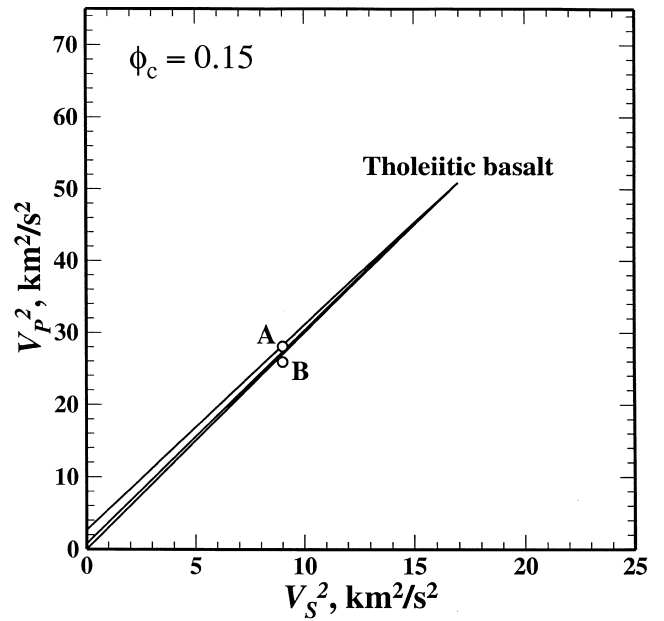


Figure 12. Empirical effect of compressible pore fluid on elastic-wave speeds in rocks, after Krief *et al.* (1990). Each line corresponds to rocks with a fixed mineralogy and pore fluid, but varying porosity ϕ . At the right end of each line, $\phi = 0$ and the elastic-wave speeds V_p and V_s take the values of the minerals in the rock matrix. The left end of each line corresponds to a cohesionless suspension of mineral particles in the pore fluid, with a 'porosity' ϕ_c . For intermediate porosity values, V_p^2 and V_s^2 lie close to the straight lines shown. The lines correspond to liquid-water pore fluid at 200°C (upper) and 300°C (middle), and to water-vapour pore fluid (lower). Point A: typical values measured in the Hengill–Grensdalur area at 2 km depth. Point B: values at the same depth within the negative V_p/V_s anomaly beneath the hot springs. No realistic mineral moduli can produce a V_p/V_s anomaly of -4 per cent by varying only the pore-fluid compressibility. The lines are computed assuming the minerals are Poisson solids with the compressibilities given by Birch (1966, Table 7–10) and using the compressibilities of water at 12.5 MPa (Grant, Donaldson & Bixley 1982, Fig. A3.2) and water vapour (Grant *et al.* 1982, Eq. A2.20 and Fig. A3.3).

observed anomaly, however, must be the combined effect of several factors, including temperature, variations in mineralogy, probably caused by geothermal alteration, and perhaps also the presence of vapour.

The assumptions made in this analysis are conservative. Different assumptions would make the anomaly harder to explain entirely as a pore-fluid effect. It is likely that the mineral moduli are lower than those we have used, because rocks exposed at the surface exhibit extensive geothermal alteration. Thus the mineral point in Fig. 12 probably should be much closer to the observed points, and the separation between the different lines should be correspondingly smaller. Assuming a higher pore pressure than 12.5 MPa lessens the effect of temperature on fluid compressibility. The value $\phi_c = 0.15$ for the porosity at which the rock becomes a cohesionless suspension is a lower bound; the actual porosities measured in drill cores are occasionally as high as 0.15 (Bodvarsson *et al.* 1990) and even higher values are reported for surface rocks. Furthermore, V_s does not anywhere approach zero as it would if ϕ_c were really 0.15. Using a larger value for

ϕ_c makes V_p less sensitive to pore-fluid compressibility, and strengthens our conclusion that a combination of effects is required.

4 NON-DOUBLE COUPLE EARTHQUAKES

4.1 Introduction

Many high-quality observations have been accumulated recently of earthquakes that cannot be modelled as DCs. It is now clear that a DC mechanism is not a fundamental property of all earthquakes (Foulger & Julian 1993; Julian *et al.* 1998; Miller, Foulger & Julian 1998). Many geothermal earthquakes in particular have non-DC mechanisms, and many of the best examples come from Iceland (Klein, Einarsson & Wyss 1977; Foulger & Long 1984; Foulger 1988b; Foulger *et al.* 1989; Arnott & Foulger 1994a,b). Before the 1991 experiment described here, studies of Icelandic non-DC earthquakes used only P -wave polarities measured from analogue recordings of vertical-component seismograms. Nevertheless, these showed that some earthquakes have substantial volumetric components. In the case of the Hengill–Grensular area, these were all explosive.

4.2 Computing moment tensors

We determined focal mechanisms for the best-recorded earthquakes from the 1991 data set by applying linear programming methods to polarities and amplitudes measured from the three-component digital data. Linear programming treats systems of inequalities that involve linear operators, and can be used to determine moment tensors from any combination of seismic-wave polarity, amplitude and amplitude-ratio observations, using the robust L1 norm to measure goodness of fit (Julian 1986; Julian & Foulger 1996). In this scheme, a polarity observation provides one inequality, which constrains the theoretical amplitude to be either >0 or <0 . An amplitude or an amplitude ratio provides two inequalities, which constrain the value to lie within a range corresponding to the observational uncertainty.

We measured polarities and amplitudes of P , SH and SV waves, and inverted the polarities and ratios of amplitudes of different phases recorded at one station. The latter are insensitive to some of the propagation effects that affect amplitudes and are difficult to model, and also eliminate the need to know instrument sensitivities. We analysed 98 earthquakes that had good focal-sphere coverage (Fig. 13). Most of these occurred in the geothermal field between 1.9 and 6.0 km depth bsl. An average of 22 P - and 17 S -wave amplitudes per event were measured.

To minimize distortion by wave-propagation effects such as scattering and attenuation, we measured amplitudes from low-pass filtered seismograms. The filter used has a three-pole Butterworth response and a corner frequency of 5 Hz. This was chosen on the basis of tests with a suite of frequencies. The 5 Hz filter gave clear arrivals and high signal-to-noise ratios, yielded more usable amplitude data than other filters, and gave the best data fit (Miller 1996). Figs 14 and 15 show examples of unfiltered and filtered seismograms. For each earthquake, only phases with similar rise times and waveform shapes were used. SH and SV waves were measured from numerically rotated transverse and longitudinal horizontal components.

We corrected the amplitude measurements for the effect of the free surface, assuming a homogeneous elastic half-space, and for attenuation. In the geometrical-optics approximation, the amplitude of a body wave arriving at the surface is

$$A = A_0 R^{-1} \exp[-\pi f t / Q], \quad (2)$$

where A_0 is the radiated amplitude normalized to a unit distance from the source, R is the geometrical spreading coefficient, f is frequency, t is traveltime and Q is the ‘figure of merit’, a characteristic of the propagation medium. The ratio of the radiated P - and S -wave amplitudes is therefore

$$\begin{aligned} \frac{A_{P_0}}{A_{S_0}} &= \frac{A_P R_P}{A_S R_S} \exp \left[\pi f \left(\frac{t_P}{Q_P} - \frac{t_S}{Q_S} \right) \right] \\ &= \frac{A_P R_P}{A_S R_S} \exp \left[\pi f \frac{t_P}{Q_P} \left(1 - \frac{Q_P V_P}{Q_S V_S} \right) \right], \end{aligned} \quad (3)$$

where A_P and A_S are the amplitudes of P and S waves just before they arrive at the surface (that is the observed amplitudes corrected for the effect of the surface). Here Q and V are effective values, averaged along rays. If spatial variations in V_P/V_S are small, then $R_P \approx R_S$. Computing the $P:S$ amplitude ratio at the source then requires t_P and t_S (or t_P and V_P/V_S) and estimates of Q_P and Q_S along the ray path.

Menke, Levin & Sethi (1995) measured the attenuation of P and S waves in south Iceland and found that $Q_P \approx 60$ and $Q_S \approx 95$ ($Q_P/Q_S \approx 0.63$) in the upper 4 km. This Q_P/Q_S ratio differs significantly from the commonly assumed value of 9/4, which corresponds to attenuation occurring only in shear (Knopoff 1964). For the values of Menke *et al.* (1995), attenuation has little effect on $P:S$ amplitude ratios. From eq. (3), with $f = 5$ Hz, $t_P/Q_P = 0.03$ and $V_P/V_S = 1.77$,

$$\frac{A_{P_0}}{A_{S_0}} = 0.95 \frac{A_P}{A_S}. \quad (4)$$

In contrast, if $Q_P/Q_S = 9/4$ and $t_P/Q_P = 0.03$,

$$\frac{A_{P_0}}{A_{S_0}} = 0.25 \frac{A_P}{A_S}. \quad (5)$$

To explore the effects of different assumptions, we inverted data from six earthquakes using values of $1/Q_P$ and $1/Q_S$ ranging from 0.005 to 0.035. In most cases the fit to the data is rather insensitive to this parameter (Figs 16 and 17). The data are marginally more consistent with the Q_P/Q_S values of Menke *et al.* (1995) than with $Q_P/Q_S \approx 9/4$, and using the former gives a slightly better fit to the data than using no attenuation correction at all (Fig. 17). As a result of these findings, we used $Q_P = 60$ and $Q_S = 95$ to correct amplitudes and amplitude ratios for all earthquakes. This is the first case known to us where the goodness of fit of earthquake focal mechanism has been used to study attenuation.

There are three main sources of amplitude uncertainty: instrumental sensitivities, unmodelled wave-propagation effects, and noise on seismograms. Inverting amplitude ratios eliminates the first uncertainty and greatly decreases the second. For an amplitude ratio, the fractional uncertainty is

$$\sigma_{\text{total}} = \sigma_a + \sigma_b + \sigma_p, \quad (6)$$

where σ_a and σ_b are the fractional uncertainties in the two amplitudes due to noise, and σ_p is the fractional error bound due to unmodelled propagation effects. We estimated σ_p empirically by computing the goodness of fit for a range of

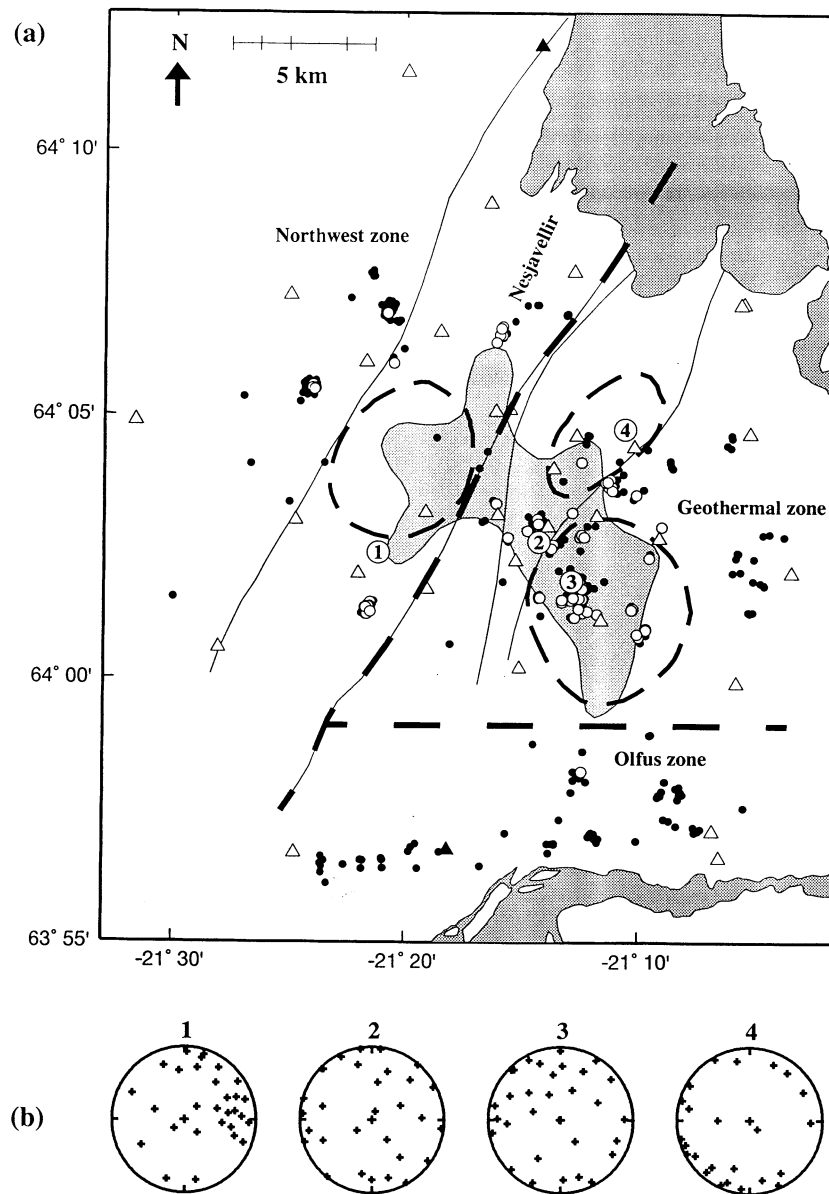


Figure 13. (a) The Hengill–Grensdalur volcanic complex. Open triangles: seismometers of the 1991 temporary network; filled triangles; seismometers of the South Iceland Lowland permanent network; dots: earthquakes; open circles: earthquakes for which moment tensors were obtained. Numbers indicate four representative earthquakes with good focal-sphere coverage. Thick dashed lines separate the three main zones of earthquake activity. (b) Upper focal hemisphere, equal-area projections of station locations for the four representative earthquakes shown in (a).

trial values. We used two measures of goodness of fit: (1) the number of polarity misfits; and (2) the mean absolute deviation (MAD) between observed and theoretical values. For the absolute deviation of an amplitude ratio we used

$$|a^{(1)} - ra^{(2)}|, \quad (7)$$

where $a^{(1)}$ and $a^{(2)}$ are the observed amplitudes and r is the theoretical ratio.

4.3 Results

We use the ‘source-type plot’ of Hudson, Pearce & Rogers (1989) to display the orientation-independent characteristics of earthquake mechanisms. This plot shows two quantities

(Fig. 18):

$$T \stackrel{\text{def}}{=} -2\varepsilon = \frac{2m'_1}{|m'_3|} \quad (8)$$

and

$$k \stackrel{\text{def}}{=} \frac{m^{(V)}}{|m^{(V)}| + |m'_3|}, \quad (9)$$

where m'_1 and m'_3 are the absolutely smallest and largest deviatoric principal moments and $m^{(V)} \stackrel{\text{def}}{=} \text{Tr}(M)/3$ is the volumetric moment. Equal areas on the plot have equal probabilities, under the *ad hoc* assumption that the principal moments are uniformly distributed in some interval. The

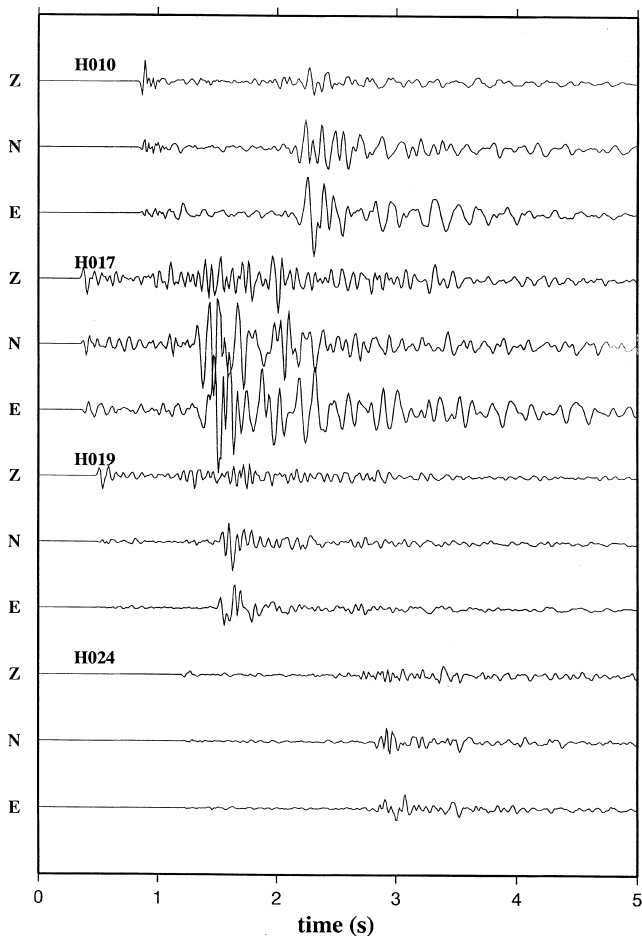


Figure 14. Representative seismograms for a well-recorded earthquake. Vertical scaling is the same at all stations.

quantity T varies from -1 on the left side of the plot to $+1$ on the right, and describes the departure of the deviatoric component from a DC. For compensated linear vector dipole (CLVD) sources, $T = \pm 1$. The quantity k varies from -1 at the bottom of the plot to $+1$ at the top, and measures the volumetric component of the mechanism. For deviatoric mechanisms, including DCs and CLVDs, $k = 0$.

On the source-type plot, any combination of a shear fault and an opening tensile crack lies within the triangle with vertices $+A$, $+Crack$ and DC (Fig. 18). Most of this triangle, however, while kinematically permissible, is dynamically improbable. If the null axis of the shear fault lies in the crack plane, then the mechanism lies along the line from $+Crack$ to DC on the left side of the triangle. Mechanisms in the right-hand portion of the triangle, however, have the T axes of the crack and the shear fault oriented very differently, so any possible stress-field orientation must be discordant with one component of the mechanism (or both). For a closing tensile crack, the situation is analogous, but the triangle is inverted with respect to the centre of the plot.

To investigate focal-mechanism resolution, we inverted 10 randomly chosen subsets of 90 per cent of the data for each event (Fig. 19) and examined the scatter in the results. The results show that k , to which $P:S$ amplitude ratios are sensitive, is much better constrained than T . Of the 98 earthquakes studied, 70 were classified as well constrained and analysed in

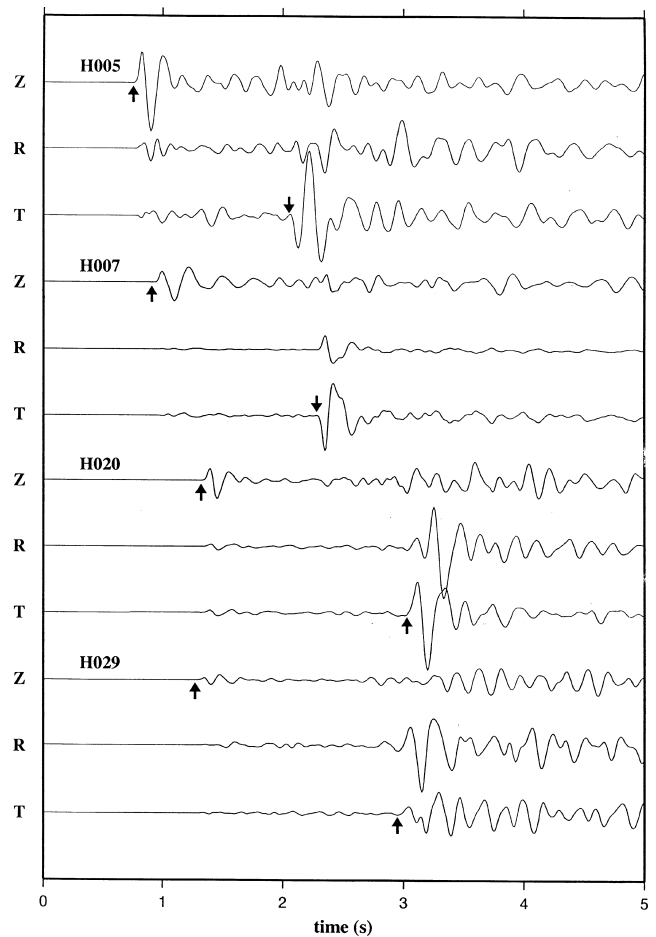


Figure 15. Representative seismograms for a well-recorded earthquake. The seismograms have been low-pass filtered with a corner frequency of 5 Hz, and the horizontal components have been rotated into radial (R) and transverse (T) orientations. Arrows show measured times and polarities of P and SH arrivals.

greater detail. For these earthquakes, some of the observed variation in k and T may be explained by error, but not all.

Most of the earthquakes studied have substantial explosive volumetric components, with k values as large as 0.42 and a mean of 0.20 (Fig. 18). Most (76 per cent) of the P -wave polarities are compressional. Only four earthquakes have implosive volumetric components (negative k) and the smallest value of k is -0.19 . For the other three implosive earthquakes k was greater than -0.1 , and probably not significant. The value of T varies from 0.8 to -0.9 . Most events (66 per cent) have $0.1 \leq k \leq 0.35$ and $-0.3 \leq T \leq 0.6$.

Most of the earthquakes have subhorizontal T axes that trend NW-SE and P -axis orientations that vary from horizontal to vertical (Fig. 20a). The plunges of the P axes increase with focal depth (Fig. 20b). The average plunge is 17° between 2 and 4 km depth, and 47° between 4 and 6 km. This pattern is similar to that reported for the 1981 data set (Foulger 1988b).

All the earthquakes for which well-constrained mechanisms were obtained have at least 14 P - and nine S -polarity observations and four amplitude ratios. The best-recorded earthquake has 27 P and 28 S polarities and 22 amplitude ratios. In local earthquake studies this many high-quality data are seldom available. To test the performance of the method

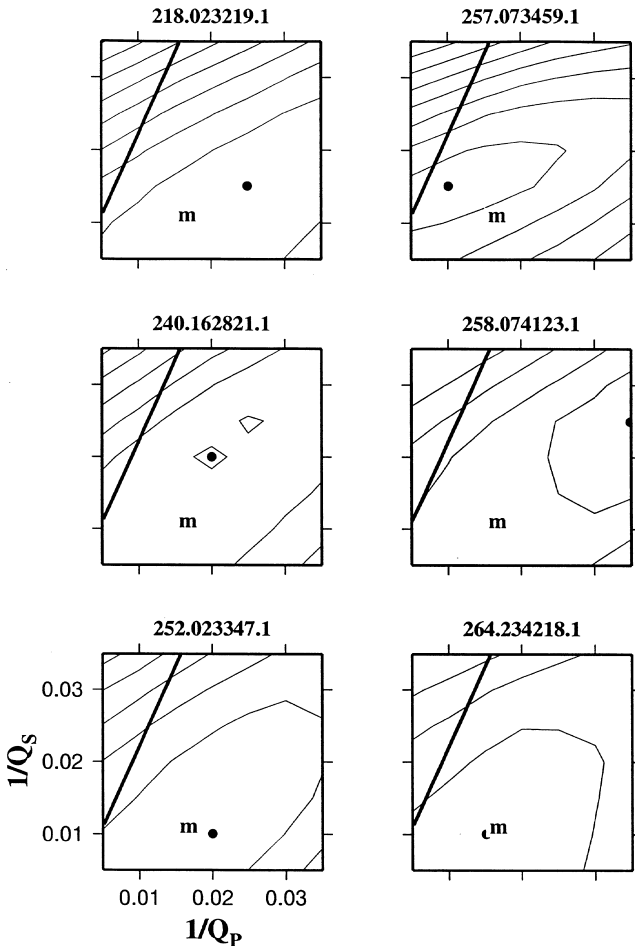


Figure 16. The effect of attenuation corrections on the goodness of fit to amplitude ratios for six earthquakes. The mean absolute deviation (dimensionless) is contoured at intervals of 0.02 for the moment tensors that result from inverting amplitude data corrected for different Q_P^{-1} and Q_S^{-1} values (also dimensionless). Points m: attenuation values of Menke *et al.* (1995); solid lines: values compatible with $Q_P = 9/4Q_S$; solid dots: the best-fit (minimum mean absolute deviation) values for each earthquake.

for sparser data, we inverted subsets of data for a trial earthquake recorded by 27 stations (Fig. 21). Only P and SH polarities and $P:SH$ amplitude ratios were used, because these data constrain the mechanism best and are also easiest to measure. With 10 or 15 well-distributed stations the solution found is similar to that for the full data set. The mechanism is clearly not a DC, and the source type and orientation are well constrained. A much wider range of solutions is possible with only five well-distributed stations, but the orientations of the principal axes are still successfully recovered. When the P -wave polarities only from all stations are inverted, a fairly wide range of mechanisms is permitted, and the most impulsive mechanism is close to a DC.

4.4. Source models

4.4.1 Shear faults

Some of the earthquakes studied here have moment tensors close to DCs. The most rigorous approach to test whether

these earthquakes are consistent with shear faulting would be to test whether a general moment tensor, with six adjustable parameters, gives a significantly better fit to data than a DC, which has four parameters. Additional degrees of freedom in the model will never give a worse data fit, but the improvement, if any, may not be significant. Such an approach is hampered by the difficulty of quantitatively assessing systematic errors, so an empirical approach was used here.

For each earthquake with $|k| < 0.2$, we compared the goodness of fit for the general moment tensor with that for the DC component of the best-fit deviatoric moment tensor. On the basis of the numbers of polarity misfits and the mean absolute deviations of the amplitude ratios, for 17 of these the evidence for a non-DC component is weak. All these possible DC mechanisms give few polarity misfits (usually less than four), and these close to nodal surfaces, and only a small increase (usually less than a factor of 2) in the mean absolute deviation, compared with the general moment tensor (Fig. 22). All of these earthquakes have $|k| < 0.3$. Figs 23(a) and (b) shows two examples.

4.4.2 Tensile–shear fault combinations

Many of the 53 well-constrained non-DC events plot within or near the field for compatible oriented tensile and shear faults (Fig. 18). Such a mechanism requires seven parameters to specify it:

- (1) the scalar moments of the shear and tensile faults (two parameters);
- (2) the orientations of the shear and tensile faults (four parameters);
- (3) the slip direction (rake) of the shear fault (one parameter).

These cannot be determined uniquely from a general moment tensor, which provides only six values. Many of the earthquakes in Fig. 18 lie near the TC–DC line, though with much scatter (especially in the $\pm T$ direction), which suggests that they may be caused by tensile–shear faulting with the T axis of the tensile crack in the T – P plane of the shear fault. Constraining the mechanism to have this geometry reduces the number of parameters required to six, but it is still difficult to compute the angle α because of trade-off between α and the relative moments of the shear and tensile fault components. Specifying the angle α between the crack and the fault (Fig. 24a) reduces the number of parameters required by two and greatly simplifies the analysis.

For $\alpha = 45^\circ$, the tensile and shear components have common principal axes (Fig. 24a). This circumstance simplifies finding the scalar moments of the tensile and shear components of the mechanism. The problem has two unknowns, the desired scalar moments, and three data, the principal moments

$$\begin{pmatrix} m_1 \\ m_2 \\ m_3 \end{pmatrix} = m^{(\text{SF})} \begin{pmatrix} 1 \\ 0 \\ -1 \end{pmatrix} + m^{(\text{TF})} \begin{pmatrix} 3 \\ 1 \\ 1 \end{pmatrix}, \quad (10)$$

and we can solve it by various *ad hoc* methods, such as least squares.

A tensile–shear combination with a restricted geometry, such as this one, has fewer adjustable parameters than a general mechanism, and so never gives a better fit to the data than a general moment tensor. However, for most of the non-DC

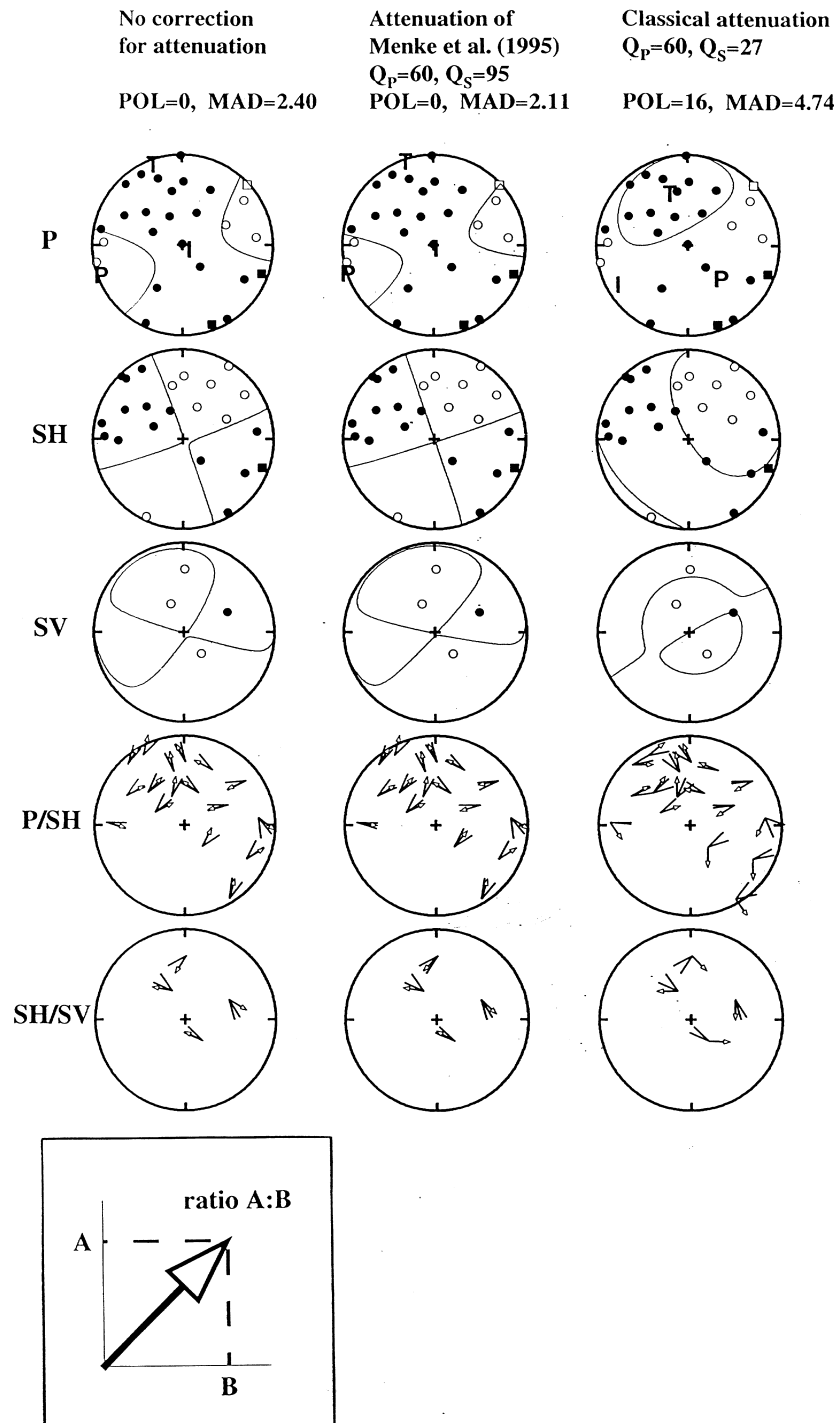


Figure 17. The effect of attenuation on the derived moment tensor for the earthquake at 07:41, 1991 September 15. Solid circles: compressions; open circles: dilatations. Amplitude ratios are depicted as vectors using the system shown at lower left. Arrows: theoretical ratios; pairs of lines: bounding values corresponding to estimated errors in the observations. The moment tensors result from inverting polarity and amplitude-ratio data with amplitude ratios corrected using different assumptions about attenuation. POL: number of *P*, *SH* and *SV* polarity misfits; MAD: mean absolute deviation; 'classical attenuation': $Q_P = 9/4Q_S$. The best fit is achieved using the values of Menke *et al.* (1995) (middle column).

earthquakes the model gives a fairly good fit to the data, with 41 out of 53 having at most three polarity misfits, and 31 having a mean absolute deviation of less than twice that of the general moment tensor. Figs 23(c)–(f) show four examples. The corresponding fault orientations are shown in Fig. 25. In many cases both shear and tensile components are aligned

approximately NE–SW, which is consistent with the local tectonic fabric.

The case $\alpha = 0$ corresponds to oblique opening on a plane (Fig. 24b). Fracture of an intact rock can cause oblique opening only under particular and probably rare stress conditions. Oblique opening on pre-existing faults may be commoner, but

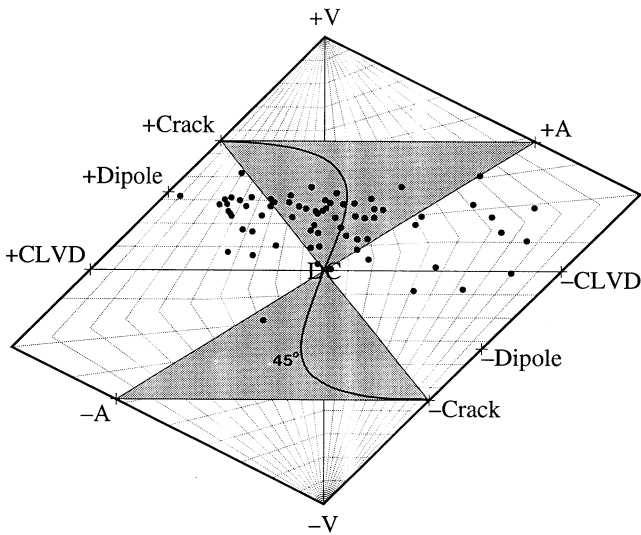


Figure 18. ‘Source-type plot’ (Hudson *et al.* 1989) of k , a measure of the volumetric component of the mechanism, against T , which measures the departure of the deviatoric part of the mechanism from a DC. k varies from +1 at the top of the plot to -1 at the bottom, and is constant along the subhorizontal gridlines, while T varies from -1 on the left-hand side to +1 on the right, and is constant along gridlines running from top to bottom. DC: double-couple; +/-Crack: opening/closing tensile cracks; +/-Dipole: force dipoles directed outwards/inwards; +/-CLVD: Compensated Linear Vector Dipoles with dominant dipoles directed outwards/inwards. Grey triangle: locus of combined tensile and shear-fault mechanisms. Solid line: boundaries of region where angle β (between the crack plane and the null axis of the shear fault) is $\leq 45^\circ$. Solid dots: the 70 well-constrained moment tensors determined for earthquakes from the Hengill–Grensdalur area.

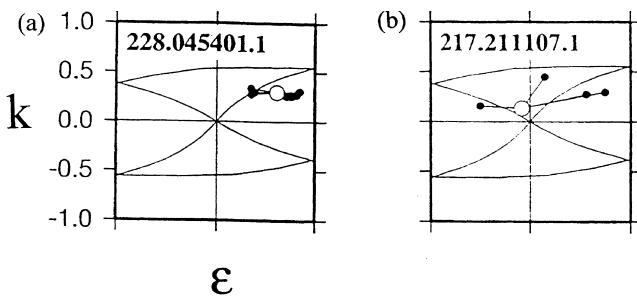


Figure 19. k - ϵ diagrams showing variations in moment tensors obtained by inverting different subsets of data. Open circles: moment tensors obtained by inverting the full data set for the earthquake; solid circles: moment tensors obtained with 10 per cent of the data removed at random. 10 such inversions were carried out for each earthquake, but not all results are identifiable on the plots, because sometimes the resulting moment tensor was exactly the same as that obtained from inverting all the data. (a) A well-constrained earthquake; (b) a poorly constrained earthquake.

some extra mechanism is required to cause such motion to be sudden rather than aseismic. In any case, the mechanism is sufficiently insensitive to α that it is probably difficult to identify decisively oblique opening using moment tensors.

The relative moments can be expressed as

$$R_{TF} \stackrel{\text{def}}{=} \frac{m^{(TF)}}{|m^{(SF)}| + |m^{(TF)}|}, \quad (11)$$

Table 2. Distribution of earthquakes interpreted as shear faulting. See Fig. 13 for location of zones.

Zone	No. of well-constrained earthquakes	Shear-fault earthquakes per cent	Mean R_{TF}
Northwest	19	37	0.10
Geothermal	50	18	0.18
Ölfus	1	100	0.07
Total:	70	24	0.16

where $m^{(SF)}$ and $m^{(TF)}$ are the scalar moments of the shear- and tensile-fault components. R_{TF} varies from -0.18 to 0.51. For all but one earthquake, the scalar moment of the shear-fault component is larger than that of the tensile-fault component. R_{TF} varies across the area, and is highest in the geothermal zone (Fig. 13, Table 2), which suggests that the non-DC processes are related to geothermal activity.

5 DISCUSSION

The consistent failure to detect bodies that might contain partial melt in the upper 6 km of crust beneath the Hengill–Grensdalur volcanic system contrasts with the situation beneath other Icelandic volcanic systems, for example the Krafla system (Einarsson 1978) and volcanoes, e.g. Hekla and Katla (Sigmundsson, Einarsson & Bilham 1992; Gudmundsson *et al.* 1994) (Fig. 1). Clearly, the shallow Icelandic crust is not devoid of partial melt, but in the upper few kilometres this may exist only as isolated bodies beneath highly active volcanoes. Krafla, Hekla and Katla have all erupted many times historically, whereas Hengill has only erupted six times in postglacial times. Eruptions from infrequently active edifices, such as Hengill and Eldfell in Heimaey, may be fed directly from magma stored at much deeper levels. The Hengill system is probably similar in structure to the systems on the Reykjanes peninsula, which appear to have more affinity to sea-floor spreading centres than to those in the interior of Iceland.

Simultaneously inverting P - and S -wave polarities and amplitude ratios is a powerful way to retrieve moment tensors for small earthquakes. Inverting subsets of data shows that 10 stations with P and SH polarities and amplitudes provide better constraint than 27 stations with P polarities only. This illustrates the advantage of deploying a few three-component seismic stations rather than many single-component instruments.

Most earthquakes in the Hengill–Grensdalur area have T axes that are aligned parallel to the local extensional direction (Fig. 20). The orientations of the P -axes vary from subhorizontal to subvertical with increasing depth. This is probably due to lithostatic increase in the vertical compressive stress. A similar variation in P -axis orientation has been reported for the Reykjanes peninsula (Klein *et al.* 1977).

The dominant mode of shear faulting in the area is probably right-lateral on NNE-striking, near-vertical faults. This agrees with the earthquakes that are consistent with a DC model, which amount to ~ 25 per cent of the well-constrained events and with the DC components of the non-DC earthquakes. It is also consistent with the tectonics of the area, the orientations of swarms relocated using master-event techniques (Miller 1996), split S -wave polarization directions (Evans *et al.* 1996)

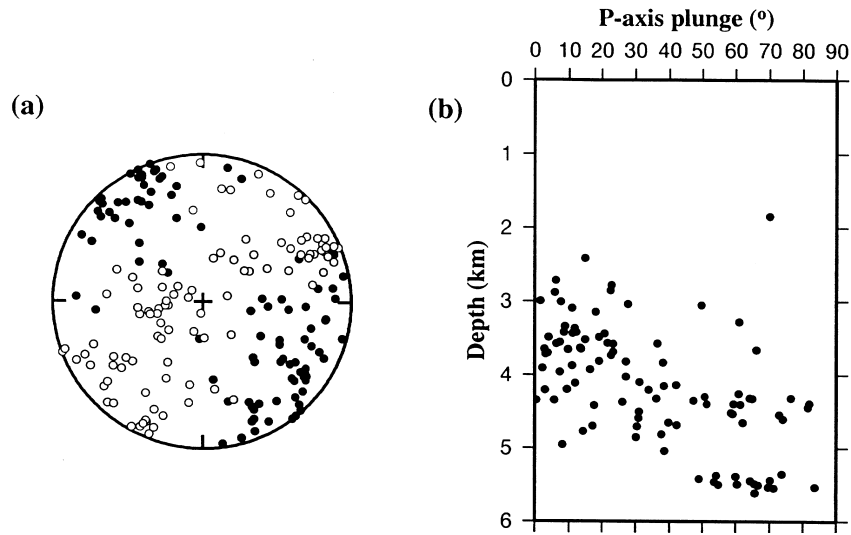


Figure 20. (a) Equal-area upper-hemisphere plots showing the orientations of *P* (open circles) and *T* (filled circles) axes for all 98 earthquakes studied. (b) Plunges of *P* axes versus earthquake depth.

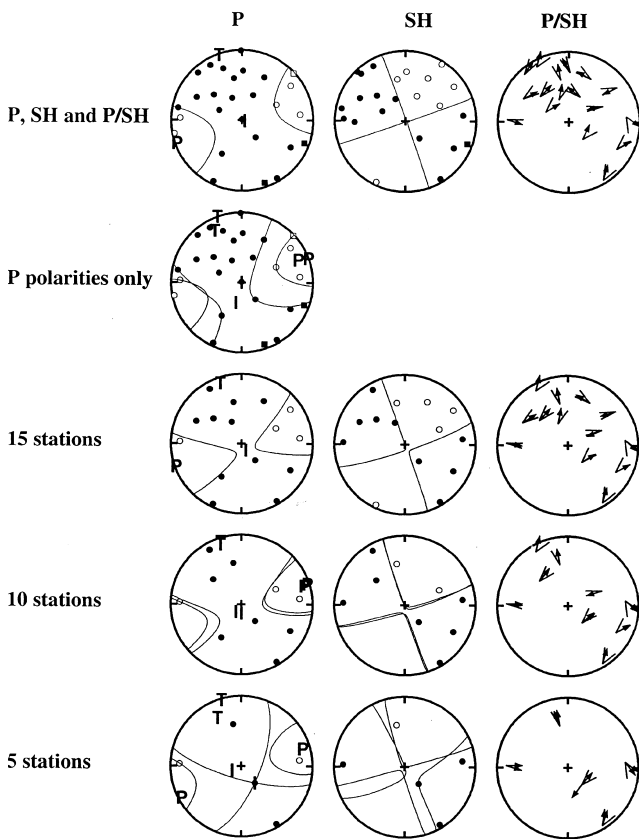


Figure 21. Moment tensors resulting from inverting different combinations of *P* and *SH* data from the earthquake at 07:41, 1991 September 15. *T*, *I* and *P*: positions of the principal axes. Where data from only a subset of stations are used, they were selected to give the best possible focal-sphere coverage. Where two sets of nodal lines are shown, they are for the most explosive and most implosive mechanisms that are compatible with the data. The use of *P* and *SH* data from 10 stations (row 4) gives better constraint than using only the *P*-wave polarities from all 27 stations (row 2).

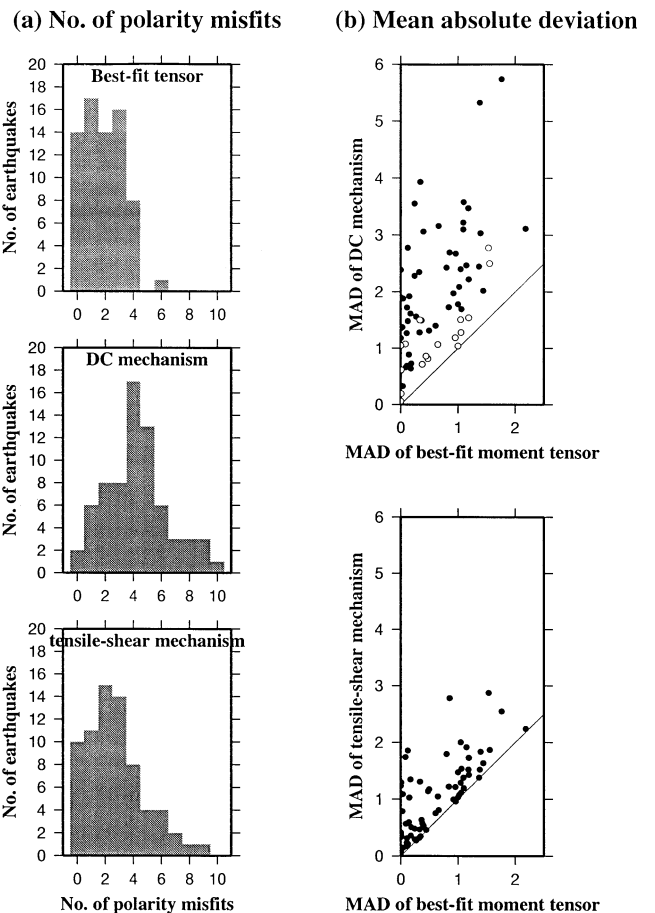


Figure 22. Comparison of goodness of fit for the best-fit moment tensor, the DC mechanism and the tensile-shear mechanism for all well-constrained earthquakes. (a) Histograms of the number of polarity misfits; (b) comparisons of the mean absolute deviations (MAD, in arbitrary units). Top: for the best-fit moment tensor and the DC mechanism. Open circles are earthquakes classified as DC. Bottom: for the best-fit moment tensor and the tensile-shear faulting mechanism.

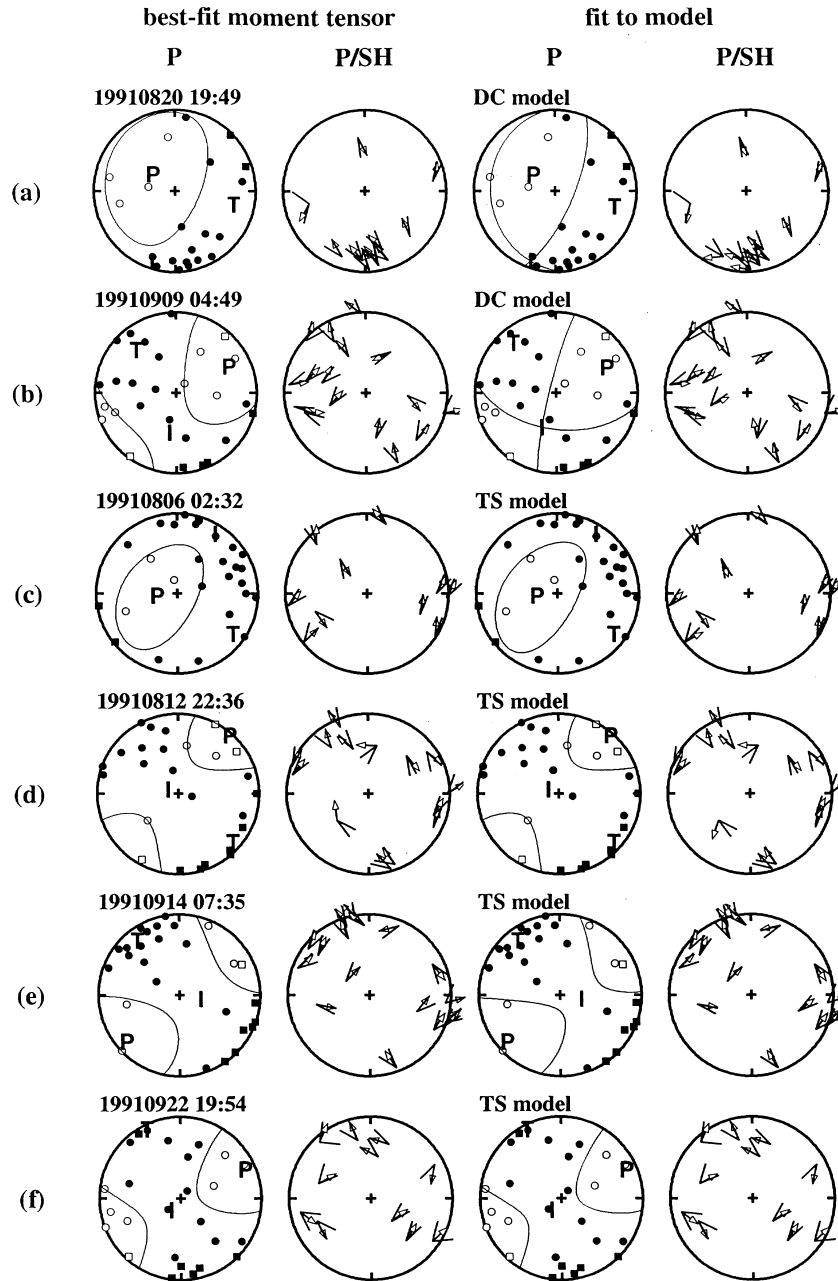


Figure 23. Example earthquakes, and the data fit to the source models considered, displayed as in Fig. 17. Two left-hand columns: P polarity and $P:SH$ amplitude ratio compared with predictions for the best-fit moment tensor. Two right-hand columns: same, for either a DC model (top two earthquakes) or a tensile–shear faulting model (TS) (bottom four earthquakes).

and observations from neighbouring systems (e.g. Klein *et al.* 1977).

The remaining 75 per cent of well-constrained earthquakes have strongly non-DC mechanisms with substantial volumetric components, explosive in most cases. Many of these events fit a model of near-simultaneous opening tensile and shear motion, and the inferred tensile cracks are generally aligned with the tectonic fabric of the area. The question arises how close together the tensile and shear faults must be in space and time. If widely separated, two P arrivals would be observed. If the fault planes are separated by 100 m, then a P wave from the first rupture would take about 0.02 s to reach the second fault. The second P arrival in this case would probably be

recognizable on seismograms. Ruptures on separate faults hundreds of metres apart would certainly produce clearly distinct P arrivals. There is no evidence of double P arrivals in the data, so it is likely that the tensile and shear faults are spatially close and rupture at times $< \sim 0.02$ s apart.

The single well-constrained earthquake with a substantial implosive component is one of a swarm beneath the geothermal wellfield at Nesjavellir, NE of Hengill, and the hypocentres were aligned along a NNE-striking plane. The first-motion directions show that the mechanisms of all the earthquakes in this sequence were similar (Fig. 26c) and the events had similar orientations of the principal axes. Candidate sources that could explain this radiation pattern include (1) a tensile–shear model,

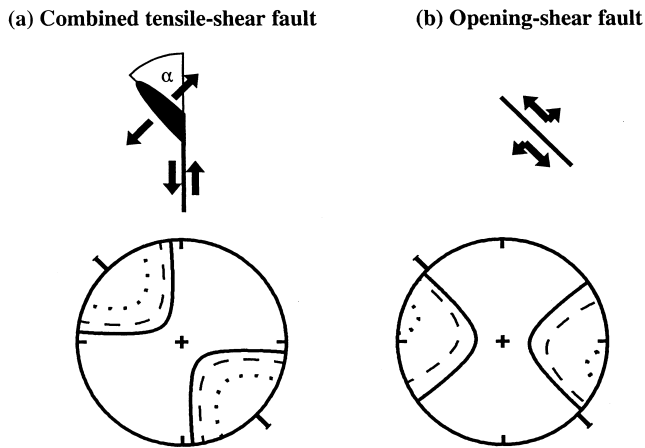


Figure 24. Candidate source mechanisms involving simultaneous tensile and shear faulting in cases where the tensile fault contains the null axis of the shear fault (the T axis of the tensile fault lies in the P - T plane of the shear fault). (a) Faulting on two separate planes. When $\alpha = 45^\circ$, the principal axes of the two components coincide. (b) Special case where $\alpha = 0$, equivalent to oblique opening of the fault. The bottom panels show equal-area projections (either upper or lower focal hemisphere) of the P -wave nodal surfaces for R_{TF} values of 0.1 (solid lines), 0.2 (dashed lines) and 0.35 (dotted lines).

with the explosive and implosive earthquakes being caused by opening and closure of orthogonal tensile faults, both accompanied by the same shearing process (Fig. 26a), and (2) opening-shear faulting, with opening and closure on similarly orientated fault planes (Fig. 26b). It is noteworthy that the only strong evidence for implosive earthquakes comes from the only exploited part of the geothermal area, and that such evidence was lacking in data collected prior to substantial exploitation, though admittedly the earlier 1981 data were relatively poor. It may be that volumetric contraction is occurring beneath the wellfield as a result of exploitation. Geodetic evidence for industrially induced volumetric contraction has recently been reported from the exploited Svartsengi geothermal area on the Reykjanes peninsula (Vadon & Sigmundsson 1997).

The events cover a broad field in the top half of the source-type plot (Fig. 18) and, although some of this spread is undoubtedly due to error, most seriously in T , it probably reflects real variation in the source mechanisms. This suggests that the DC events modelled above are members of a continuum of source types in this area. Many events lie in the improbable (right-hand) part of the TC-DC triangle or outside of it, and these must involve some additional source process. Compensation of the explosive component, perhaps by the flow of high-pressure geothermal fluids into the opening crack at the instant of fracture, and its counterpart in the case of the rare implosive events, can potentially explain all of the moment that lies outside the TC-DC triangles in Fig. 18 (Ross, Foulger & Julian 1996).

Non-DC earthquakes have been found in many areas and environments (Miller, Foulger & Julian 1998). The question then remains whether such earthquakes are unusual, or whether departures from shear faulting are common but so far only rarely recognized because recording has been poor and/or because the non-DC components are small. It is important to distinguish between non-DC radiation patterns that result

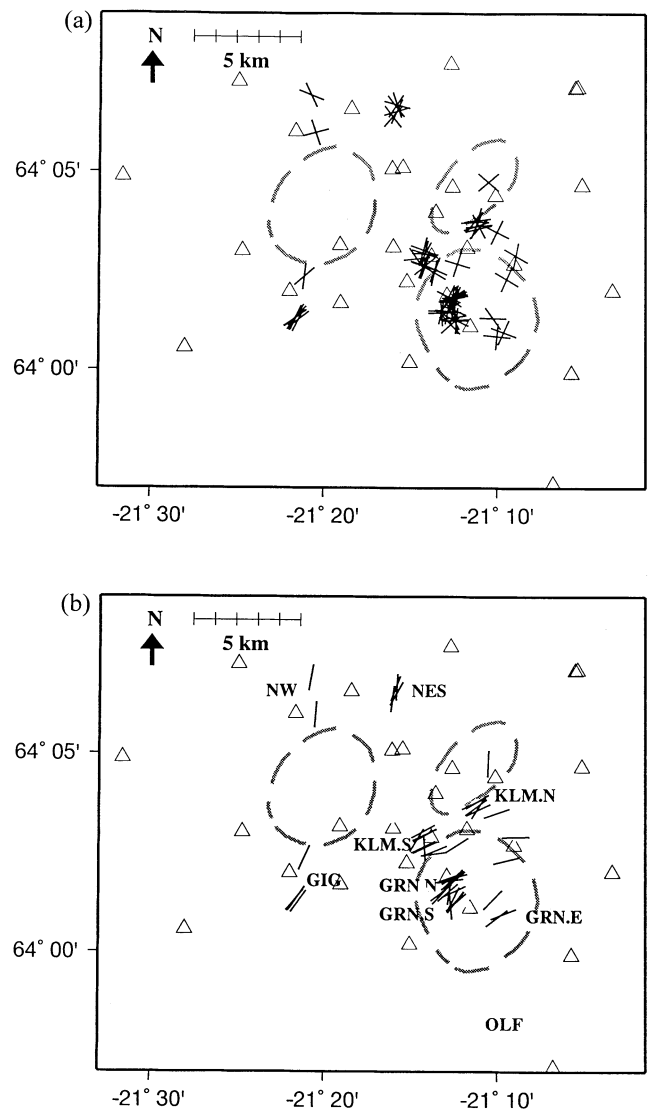


Figure 25. Inferred strike directions of the fault planes for combined tensile-shear faulting models of the well-constrained non-DC earthquakes. (a) Orientations of both nodal planes of the shear components; (b) orientations of the tensile fault planes.

from propagation effects and those that result from non-shear source processes. We concur with the view that both non-DC radiation patterns and non-shear source processes are common, and conclude that focal-mechanism studies performed in the future should discard the traditional *a priori* DC constraint, in particular for volcanic or geothermal earthquakes.

ACKNOWLEDGMENTS

The LET programs were provided by C. Thurber and D. Eberhart-Phillips. Their support and advice is greatly appreciated. IRIS/PASSCAL and NERC supplied the field equipment. Joseph Holmjarn detonated the explosion that saved the experiment, and Egill Gudmundsson encouraged it in his trout lake. Data from the SIL network were supplied by the Iceland Meteorological Office. Funding was provided by a USGS G. K. Gilbert fellowship, a NERC grant and a

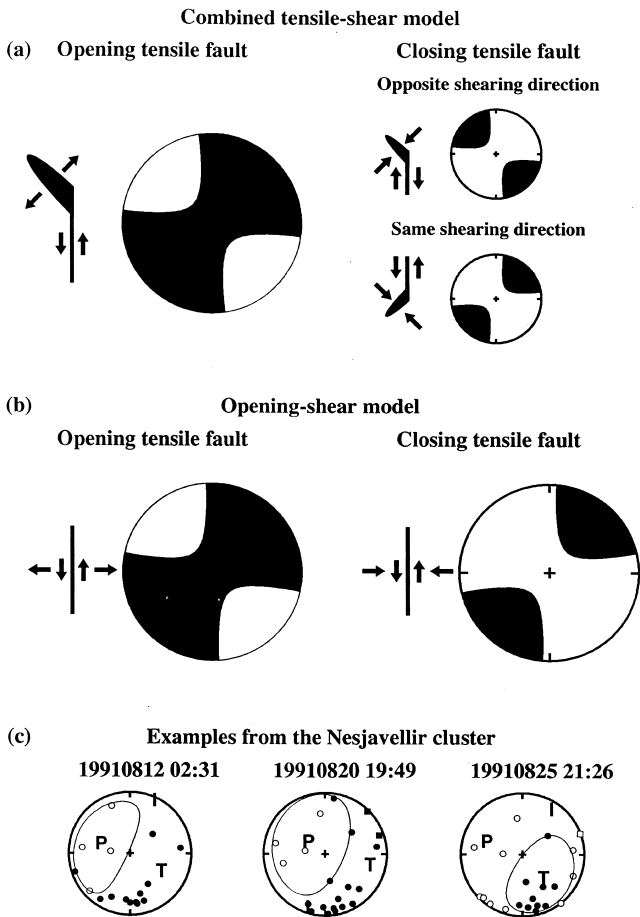


Figure 26. Comparison of mechanisms with opening and closing tensile-fault components for (a) $\alpha = 45^\circ$ and (b) $\alpha = 0$. Areas of compression are black. (c) *P* polarities and nodal lines for three earthquakes at Nesjavellir that have similar mechanisms but one of which (the right-hand one) has a substantial implosive component.

NERC studentship (ADM). The GMT mapping package (Wessel & Smith 1991) was used for data analysis and figure preparation.

REFERENCES

- Arnott, S.K. & Foulger, G.R., 1994a. The Krafla spreading segment, Iceland: 1. Three-dimensional crustal structure and the spatial and temporal distribution of local earthquakes, *J. geophys. Res.*, **99**, 23 801–23 825.
- Arnott, S.K. & Foulger, G.R., 1994b. The Krafla spreading segment, Iceland: 2. The accretionary stress cycle and non-shear earthquake focal mechanisms, *J. geophys. Res.*, **99**, 23 827–23 842.
- Birch, F., 1966. Compressibility; elastic constants, in *Handbook of Physical Constants*, revised edn, pp. 97–173, ed. Clark, S.P., Jr., Geological Society of America, New York, NY.
- Bodvarsson, G.S., Björnsson, S., Gunnarsson, A., Gunnlaugsson, E., Sigurdsson, O., Stefansson, V. & Steingrímsson, B., 1990. The Nesjavellir geothermal field, Iceland, Part 1. Field characteristics and development of a three-dimensional numerical model, *Geotherm. Sci. Tech.*, **2**, 189–228.
- Chatterjee, S.N., Pitt, A.M. & Iyer, H.M., 1985. V_p/V_s ratios in the Yellowstone National Park Region, Wyoming, *J. Volc. Geotherm. Res.*, **26**, 213–230.

- Eberhart-Phillips, D., 1993. Local tomography: earthquake source regions, in *Seismic Tomography: Theory and Practice*, pp. 613–643, eds Iyer, H.M. & Hirahara, K., Chapman & Hall, London.
- Einarsson, P., 1978. S-wave shadows in the Krafla caldera in NE-Iceland, evidence for a magma chamber in the crust, *Bull. Volc.*, **41**, 1–9.
- Evans, J.R., Foulger, G.R., Julian, B.R. & Miller, A.D., 1996. Crustal shear-wave splitting from local earthquakes in the Hengill triple junction, southwest Iceland, *Geophys. Res. Lett.*, **23**, 455–458.
- Foulger, G.R., 1988a. The Hengill triple junction, SW Iceland. 1. Tectonic structure and the spatial and temporal distribution of local earthquakes, *J. geophys. Res.*, **93**, 13 493–13 506.
- Foulger, G.R., 1988b. The Hengill triple junction, SW Iceland. 2. Anomalous earthquake focal mechanisms and implications for processes within the geothermal reservoir at accretionary plate boundaries, *J. geophys. Res.*, **93**, 13 507–13 523.
- Foulger, G.R. & Julian, B.R., 1993. Non-double-couple earthquakes at the Hengill-Grensdalur Volcanic Complex, Iceland: Are they the artifacts of crustal heterogeneity?, *Bull. seism. Soc. Am.*, **83**, 38–52.
- Foulger, G. & Long, R.E., 1984. Anomalous focal mechanism solutions: evidence for tensile crack formation on an accreting plate boundary, *Nature*, **310**, 43–45.
- Foulger, G.R. & Toomey, D.R., 1989. Structure and evolution of the Hengill-Grensdalur central volcano complex, Iceland: Geology, geophysics and seismic tomography, *J. geophys. Res.*, **94**, 17 511–17 522.
- Foulger, G.R., Long, R.E., Einarsson, P. & Björnsson, A., 1989. Implosive earthquakes at the active accretionary plate boundary in Iceland, *Nature*, **337**, 640–642.
- Foulger, G.R., Miller, A.D., Julian, B.R. & Evans, J.R., 1995. Three-dimensional V_p and V_p/V_s structures of the Hengill triple junction and geothermal area, Iceland and the repeatability of tomographic inversions, *Geophys. Res. Lett.*, **22**, 1309–1312.
- Grant, M.A., Donaldson, I.G. & Bixley, P.F., 1982. *Geothermal Reservoir Engineering*, Academic Press, New York, NY.
- Gudmundsson, O., Brandsdóttir, B., Menke, W. & Sigvaldason, G.E., 1994. The crustal magma chamber of the Katla volcano in south Iceland revealed by 2-D seismic undershooting, *Geophys. J. Int.*, **119**, 277–296.
- Hudson, J.A., Pearce, R.G. & Rogers, R.M., 1989. Source type plot for inversion of the moment tensor, *J. geophys. Res.*, **94**, 765–774.
- Julian, B.R., 1986. Analysing seismic-source mechanisms by linear-programming methods, *Geophys. J. R. astr. Soc.*, **84**, 431–443.
- Julian, B.R. & Foulger, G.R., 1996. Earthquake mechanisms from linear-programming inversion of seismic-wave amplitude ratios, *Bull. seism. Soc. Am.*, **86**, 972–980.
- Julian, B.R. & Gubbins, D., 1977. Three-dimensional seismic ray tracing, *J. Geophys.*, **43**, 95–113.
- Julian, B.R., Ross, A., Foulger, G.R. & Evans, J.R., 1996. Three-dimensional seismic image of a geothermal reservoir: The Geysers, California, *Geophys. Res. Lett.*, **23**, 685–688.
- Julian, B.R., Miller, A.D. & Foulger, G.R., 1997. Non-double-couple earthquakes at the Hengill-Grensdalur geothermal area, southeast Iceland, *Geophys. Res. Lett.*, **24**, 743–746.
- Julian, B.R., Miller, A.D. & Foulger, G.R., 1998. Non-double-couple earthquakes I. Theory, *Rev. Geophys.*, in press.
- Kissling, E., Ellsworth, W.L., Eberhart-Phillips, D. & Kradolfer, U., 1994. Initial reference models in local earthquake tomography, *J. geophys. Res.*, **99**, 19 635–19 646.
- Klein, F.W., Einarsson, P. & Wyss, M., 1977. The Reykjanes Peninsula, Iceland, earthquake swarm of September 1972 and its tectonic significance, *J. geophys. Res.*, **82**, 865–887.
- Knopoff, L., 1964, *Q. Rev. Geophys.*, **2**, 625–660.
- Krief, M., Garat, J., Stellingwerff, J. & Ventre, J., 1990. A petrophysical interpretation using the velocities of *P* and *S* waves, *Log Analyst*, **31**, 355–369.
- Menke, W., Levin, V. & Sethi, R., 1995. Seismic attenuation in the crust at the mid-Atlantic plate boundary in south-west Iceland, *Geophys. J. Int.*, **122**, 175–182.

- Miller, A.D., 1996. Seismic structure and earthquake focal mechanisms of the Hengill volcanic complex, S.W. Iceland, *PhD thesis*, University of Durham, Durham.
- Miller, A.D., Foulger, G.R. & Julian, B.R., 1998. Non-double-couple earthquakes II. Observations, *Rev. Geophys.*, in press.
- O'Connell, D.R.H., 1986. Seismic velocity structure and micro-earthquake source properties at The Geysers, California, geothermal area, *PhD thesis*, University of California, Berkeley, CA.
- Ross, A., Foulger, G.R. & Julian, B.R., 1996. Non-double-couple earthquake mechanisms at The Geysers geothermal area, California, *Geophys. Res. Lett.*, **23**, 877–880.
- Saemundsson, K., 1995a. Hengill, geological map (bedrock) 1:50 000, Orkustofunun, Hitaveita Reykjavíkur, Landmaelingar Islands.
- Saemundsson, K., 1995b. *Hengill, Jarðhiti, Ummyndun og Grunnvatn*, 1:25 000, (Hengill, Geothermal, Alteration and Groundwater, 1:25 000), Orkustofunun, Hitaveita Reykjavíkur, Landmaelingar Islands.
- Sigmundsson, F., Einarsson, P. & Bilham, R., 1992. Magma chamber deflation recorded by the Global Positioning System: The Hekla 1991 eruption, *Geophys. Res. Lett.*, **19**, 1483–1486.
- Thurber, C.H., 1983. Earthquake locations and three-dimensional crustal structure in the Coyote Lake area, central California, *J. geophys. Res.*, **88**, 8226–8236.
- Thurber, C.H., 1993. Local earthquake tomography: velocities and V_p/V_s -theory in *Seismic Tomography: Theory and Practice*, pp. 563–583, eds Iyer, H.M. & Hirahara, K., Chapman & Hall, London.
- Toomey, D.R. & Foulger, G.R., 1989. Inversion of local earthquake data from the Hengill-Grensdular Central Volcanic complex, Iceland, *J. geophys. Res.*, **94**, 17 497–17 510.
- Torfason, H., Hersir, G.P., Saemundsson, K., Johnsen, G.V. & Gunnlaugsson, E., 1983. Vestur-Hengill. Yfirbordsrannsókn jarðhitasvaedisins. (West Hengill. Surface research of the geothermal area), *Nat. Energy Auth., Reykjavik, Iceland*, Rep. OS-83119/JHD-22.
- Vadon, H. & Sigmundsson, F., 1997. Crustal deformation from 1992 to 1995 at the mid-Atlantic ridge, southwest Iceland, mapped by satellite radar interferometry, *Science*, **275**, 193–197.
- Wessel, P. & Smith, W.H.F., 1991. Free software helps map and display data, *EOS, Trans. Am. geophys. Un.*, **72**, 441, 445–446.